Chemical Engineering Journal 526 (2025) 171212

Contents lists available at ScienceDirect

Chemical Engineering Journal

journal homepage: www.elsevier.com/locate/cej

# Balancing stripping/plating kinetics by bio-inspired voltage gating of ion flux rectification for dendrite-free Zn anodes

Tianyu Zhang [a,1], Feng Yang [b,1], Yuexin Liu [a], Chengcheng Dong [a], Hongfei Wang [b,*], Yong Hu [a,*]

[a] Institute of Nanocatalysis and Energy Conversion, College of Chemistry and Materials Engineering, Zhejiang A&F University, Hangzhou, 311300, China
[b] Key Laboratory of the Ministry of Education for Advanced Catalysis Materials, Department of Chemistry, Zhejiang Normal University, Jinhua, 321004, China

ARTICLE INFO

*Keywords:*
CMC
CTAB
Stripping and plating kinetics
Ion flux rectification
Dendrite-free Zn anode

ABSTRACT

Current interfacial engineering strategies for stabilizing Zn anodes, such as regulating metal stripping, promoting desolvation of hydrated $Zn^{2+}$ complexes, and seeding nucleation, often fail to synergistically control Zn stripping/plating kinetics. To overcome this limitation, we report a bioinspired voltage-gated protective layer (VGPL) constructed on a Zn anode (denoted as VGPL@Zn), using carboxymethyl cellulose (CMC) and cetyltrimethylammonium bromide (CTAB) as a model system. This VGPL@Zn functions as an ion flux rectifier to kinetically balance Zn stripping and plating processes. During stripping under a positive interfacial electric field, CTAB dynamically detaches from the protective layer. The remaining CMC matrix electrostatically repels $SO_4^{2-}$ anions, thereby suppressing parasitic reactions while simultaneously facilitating efficient Zn dissolution. Upon electric field reversal during plating, CTAB re-integrates into the protective layer. Its vertically aligned hydrophobic alkyl chains promote desolvation, while the oxygen-rich groups in CMC molecules act as zincophilic sites to guide subsequent nucleation. This dynamic protection mechanism ensures stable ion flux during both half-cycles, endowing symmetric cells with remarkable dendrite-free cycling of operation for 5568 h at 5 mA $cm^{-2}$/1 mAh $cm^{-2}$. Moreover, a VGPL@Zn//$Zn_{0.25}V_2O_5$ full cell exhibits outstanding capacity retention of 87.1 % over 1000 cycles. This dynamic interface engineering strategy enables robust Zn anodes with significant potential for practical applications.

## 1. Introduction

The rapid expansion of portable electronics and electric vehicles has intensified the demand for cost-effective and reliable energy storage systems that surpass conventional Li-ion batteries (LIBs), which rely on flammable organic electrolytes [1,2]. Within the spectrum of alternative techniques, Zn-ion batteries (ZIBs) have emerged as a promising candidate due to their intrinsically nonflammable aqueous electrolytes and inherent safety advantages [3–7]. Nevertheless, the practical deployment of ZIBs faces substantial limitations arising from the electrochemical instability of Zn metal anodes in aqueous electrolyte environments. The highly polar water molecules, characterized by their small molecular size, readily coordinate with $Zn^{2+}$ ions and engage in parasitic reactions during Zn stripping/plating cycling [8–11]. These undesirable electrochemical processes primarily consist of competitive hydrogen evolution reactions (HER) and anode corrosion [12–14]. More critically, uncontrolled Zn dendrite formation represents a fundamental limitation in ZIB systems, manifesting as depressed Coulombic efficiencies (CEs) and rapid capacity fade [15–17]. Therefore, the rational design of the anode/electrolyte interface reaction is paramount for developing commercially viable ZIBs with long-lasting cycle life.

Generally, there are currently three main strategies to control the surface morphology of Zn metal after cycling, particularly through interfacial engineering via protective coatings [18–20], advanced electrolyte formulations employing functional additives or quasi-solid-state hydrogels [6,21,22], and structural modifications ranging from three-dimensional (3D) current collector architectures to crystallographic orientation manipulation [23,24]. Among various stabilization approaches, constructing artificial interfacial layers has emerged as a particularly efficient and operationally simple strategy for Zn anode

* Corresponding authors.
*E-mail addresses:* whf0614@zjnu.edu.cn (H. Wang), yonghu@zafu.edu.cn (Y. Hu).
*URL*: https://www.x-mol.com/groups/yonghu (Y. Hu).
[1] These authors contributed equally to this work.

https://doi.org/10.1016/j.cej.2025.171212
Received 1 October 2025; Received in revised form 4 November 2025; Accepted 23 November 2025
Available online 24 November 2025

protection. These engineered interfaces serve as multifunctional nano-regulators that modulate ionic flux distribution and homogenize electric fields, enabling spatially uniform Zn deposition [25,26]. The dissolution, desolvation, and nucleation energetics constitute the three pivotal reaction processes governing the longevity of Zn anodes in rechargeable battery systems [27,28]. However, current interfacial engineering research focuses predominantly on isolated performance enhancements, such as accelerating dissolution, reducing desolvation energy, or improving nucleation uniformity, rather than adopting a holistic approach. Achieving efficient Zn metal utilization by balancing the kinetics of stripping and plating processes remains a significant challenge. Regarding the actual issues at Zn anode, excessive accumulation of counteranions ($SO_4^{2-}$, $CF_3SO_3^-$, etc.) in the electric double layer during the Zn stripping phase can lead to the formation of "dead Zn", which not only reduces active Zn content but also disrupts interfacial ion flux homogeneity [29,30]. Moreover, the $[Zn(H_2O)_6]^{2+}$ solvation shell necessitates substantial energy consumption for desolvation before deposition [31,32]. Correspondingly, progressive $Zn^{2+}$ depletion establishes pronounced concentration gradients within the anode/electrolyte interface. The resulting concentration polarization drives localized $Zn^{2+}$ flux accumulation at surface protrusions, creating an autocatalytic process that dramatically accelerates dendritic growth [33,34]. Developing integrated strategies that simultaneously optimize Zn stripping/plating reaction kinetics while suppressing dendritic growth emerges as a critical research imperative for advancing ZIB technologies.

In vivo, numerous cell types, including neurons and various muscle

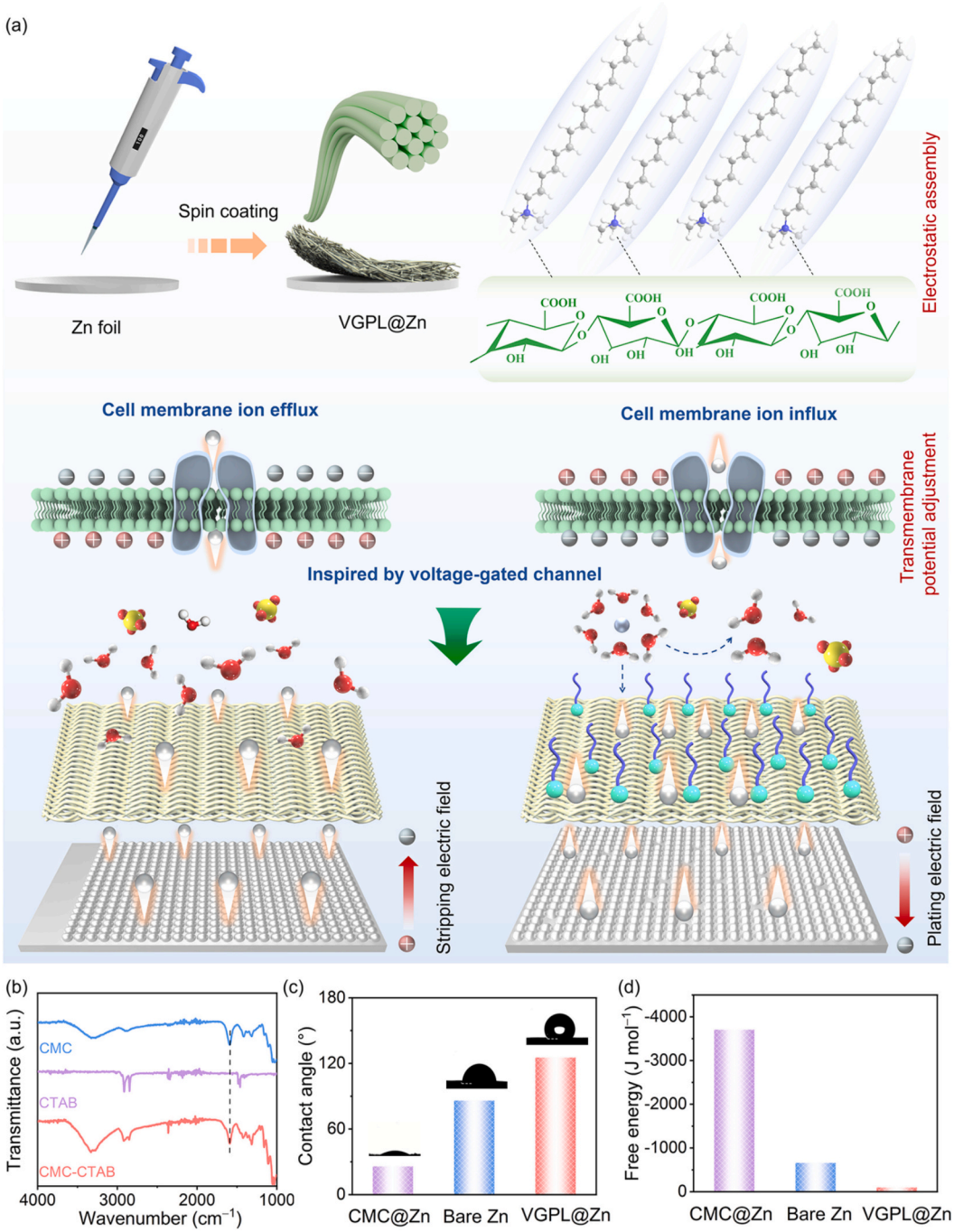


**Fig. 1.** (a) Schematic illustration of the preparation of the VGPL@Zn electrode and its regulation mechanism on the stripping/plating process. (b) FTIR spectra of CMC, CTAB, and CMC-CTAB. (c) Contact angles of CMC@Zn, bare Zn, and VGPL@Zn. (d) Wetting Gibbs free energy of CMC@Zn, bare Zn, and VGPL@Zn.

cells, possess an array of voltage-gated channel proteins embedded within their plasma membranes [35]. These sophisticated proteins can dynamically open their channels in response to localized changes in membrane potential, thereby regulating stable transmembrane ion fluxes. Similarly, the interfacial voltage can switch in tandem with the transition between the charging and discharging processes in ZIBs. Therefore, this biological mechanism may inspire an ingenious strategy to address the chaotic Zn stripping/deposition processes by designing an artificial voltage-gated channel as a "$Zn^{2+}$ rectifier" at the anode/electrolyte interface [36,37].

In this work, we engineered a bioinspired voltage-gated protective layer on the Zn anode through electrostatic self-assembly of carboxymethyl cellulose nanofiber (CMC) and cetyltrimethylammonium bromide (CTAB) as a model system, designated as VGPL@Zn (Fig. 1a). As designed, this composite coating functions as an ion rectification layer, dynamically modulating its components in response to voltage variations during charge/discharge cycles. In the Zn stripping stage, CTAB detaches dynamically from the Zn anode surface under the influence of the positive electric field. The remaining CMC component then effectively repels $SO_4^{2-}$ anions away from the Zn anode interface and induces rapid Zn stripping from the electrode surface, thereby minimizing the accumulation of by-products on the Zn electrode. During Zn deposition, the electric field reversal triggers the re-emergence of CTAB, where the vertically aligned hydrophobic alkyl chains efficiently facilitate the desolvation of hydrated $Zn^{2+}$ ions. Meanwhile, the oxygen-rich functional groups in CMC promote highly efficient Zn nucleation. This dynamically adaptive interfacial layer facilitates rapid charge transfer kinetics and balances Zn stripping/plating reactions. The symmetric cell employing VGPL@Zn electrodes demonstrates exceptional cycling stability, sustaining dendrite-free operation for 5568 h at 5 mA $cm^{-2}$/1 mAh $cm^{-2}$. Furthermore, the modified anode maintains an outstanding average CE of 99.7 % throughout cycling. The full battery configuration pairing the VGPL@Zn anode with the $Zn_{0.25}V_2O_5$ cathode (ZVO) exhibits exceptional cycling stability, retaining 87.1 % of its initial capacity after 1000 cycles at 10 A $g^{-1}$.

## 2. Results and discussion

### 2.1. Synthesis and characterization of VGPL

The VGPL@Zn electrode was synthesized using a spinning-coating method. The optical photograph demonstrates that the VGPL@Zn electrode possesses a black-coated surface (Fig. S1a). Data from micrometer measurements determine the thickness of this protective layer to be approximately 47 μm (Fig. S1b). The morphology characterization of the protective layer was performed using scanning electron microscopy (SEM), $N_2$ adsorption/desorption measurements, and energy-dispersive X-ray spectroscopy (EDS) elemental mapping. Microscopic analysis reveals the formation of a 3D hierarchical porous interfacial layer on the Zn substrate (Fig. S2). $N_2$ physisorption analysis further demonstrates the coexistence of mesopores and macropores in the protective layer composite, as evidenced by its type IV adsorption-desorption isotherm and pore size distribution profile (Fig. S3). The material exhibits a calculated specific surface area of 8.6 $m^2$ $g^{-1}$. These textural properties confirm the development of a well-defined porous architecture, which is expected to facilitate controlled $Zn^{2+}$ transport through the protective layer matrix. Additionally, EDS mapping demonstrates a homogeneous spatial distribution of C, N, and O elements (Fig. S4), indicating the effective formation of a composite layer comprising both CMC and CTAB molecules on the Zn electrode surface. Zeta potential measurements in Fig. S5 verify partial charge neutralization through electrostatic self-assembly, as confirmed by the altered surface potential (−23.7 mV) of the CMC-CTAB complex compared to its components (CMC: −27.9 mV and CTAB: +21.9 mV).

The molecular structure and chemical composition of the composite protective layer were systematically examined using Fourier transform infrared spectroscopy (FTIR) and X-ray photoelectron spectroscopy (XPS). FTIR spectral analysis (Fig. 1b) reveals two distinct peaks at 3310 and 1598 $cm^{-1}$, corresponding to the characteristic hydroxyl –OH stretching vibration and carboxyl –COOH stretching vibration of CMC, respectively. Another three absorption peaks at 2923, 2859, and 1460 $cm^{-1}$ are also detected in the CMC-CTAB spectrum. These peaks are assigned to the symmetric stretching of $–CH_3$, the asymmetric stretching of $–CH_2$, and the bending vibration of $–C–N^+$ groups from CTAB, respectively [38]. Compared to pure CMC, a blue shift in the carboxyl –COOH stretching vibration peak (from 1591 to 1598 $cm^{-1}$) is observed in the CMC-CTAB composite. This wavenumber shift provides direct spectroscopic evidence for the establishment of strong electrostatic interactions between CMC and CTAB molecules. Surface chemical measurements were performed through XPS, revealing the existence of C, N, and O elements in the CMC-CTAB composite (Fig. S6a) [39]. As shown in Fig. S6b, the corresponding O 1 s spectra display two well-resolved components at 531.6 and 532.4 eV, attributed to C═O bonds and C—O species, respectively. The O 1 s peak of CMC-CTAB exhibits a shift toward lower binding energy relative to CMC, which is also associated with the electrostatic assembly [40].

The surface free energy of VGPL@Zn was further evaluated by determining its liquid-solid contact angle values using the Owens-Wendt-Kaelble method. Interfacial wettability analysis in Fig. 1c reveals that the Zn electrode modified with pure CMC exhibits pronounced hydrophilicity (contact angle: 26.0°), whereas modification with CMC-CTAB significantly enhances the hydrophobicity of the electrode surface (contact angle: 125.6°). These results confirm that the cooperative assembly of the two components successfully constructs a more hydrophobic surface by exposing the aliphatic chains of CTAB. Accordingly, the wetting surface free energy based on Eq. S1 in Fig. 1d undergoes a pronounced reduction following CMC-CTAB functionalization (−102.8 J $mol^{-1}$), confirming the weakened interfacial interactions. This altered surface energy creates a favorable condition for desolvation, as the reduced solvent affinity promotes easier $Zn^{2+}$ detachment from solvation shells. Therefore, this CMC-CTAB composite protective layer, leveraging the complementary functionalities of both components, is expected to establish an optimized interface that effectively suppresses dendrite formation and side reactions, thereby enhancing the cycling stability of Zn anodes.

### 2.2. Measurements of Zn plating/stripping durability

Continuous cycling frequently induces detrimental dendrite formation and by-product accumulation, substantially compromising the electrochemical reversibility of Zn anodes. To quantitatively assess stripping/plating reversibility, CE measurements were conducted using either conventional Cu//Zn or modified VGPL@Cu//Zn asymmetric configurations. Fig. 2a compares Zn stripping/plating CE in asymmetric cells employing different electrodes under standardized conditions (2 mA $cm^{-2}$ and 1 mAh $cm^{-2}$). A higher initial CE value of 97.7 % was measured for the VGPL@Cu//Zn cell, versus 96.8 % for the Cu//Zn cell (Fig. S7). This is a result of the protective layer optimizing the electric field distribution across the electrode surface, thus enabling stable initial Zn plating/stripping behavior. The VGPL@Cu//Zn cell stably operates 1250 cycles with exceptional reversibility (average CE = 99.7 %). Nevertheless, the control Cu//Zn half-cell delivers limited cycling stability, failing after only 150 cycles due to dendritic penetration of the separator. The negligible variation observed in voltage profiles during cycling (Fig. S8) also verifies the VGPL@Cu electrode's ability to facilitate a highly stable Zn stripping/plating process. Comparative analysis reveals the modified cell's superior kinetics, exhibiting a reduced overpotential of 66.7 mV compared to 71.2 mV for the untreated Zn//Cu system. This performance enhancement substantiates improved $Zn^{2+}$ transport kinetics, attributable to the interfacial stabilization effect provided by the composite protective layer [41].

The symmetric cell test could be an efficient and practical method for

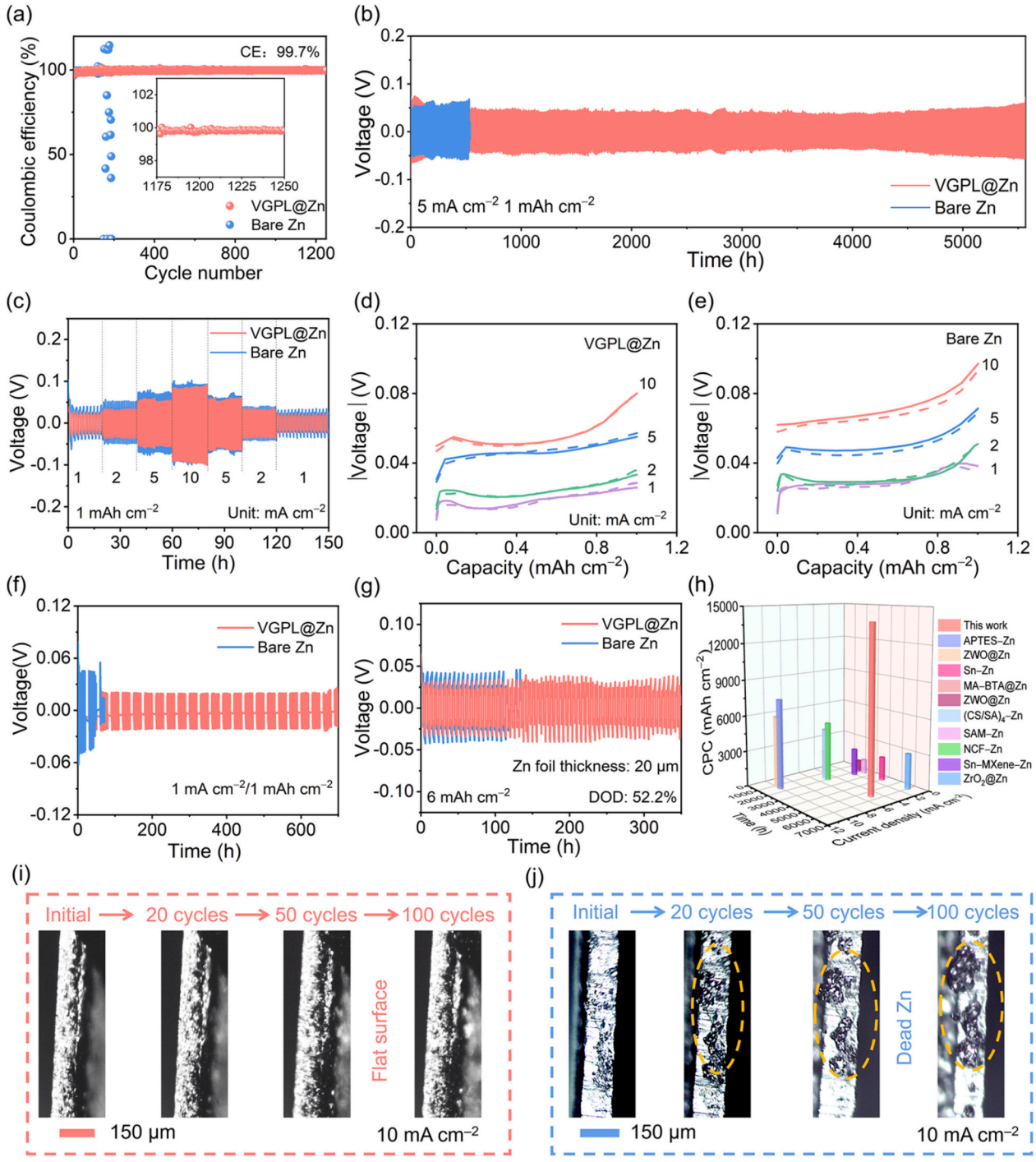


**Fig. 2.** (a) CE of asymmetric cells. (b) Cycling performances of symmetric cells at 5 mA $cm^{-2}$/1 mAh $cm^{-2}$. (c) Rate performances. Charge-discharge curves of (d) VGPL@Zn and (e) bare Zn symmetric cells. (f) Electrochemical behaviors of symmetric cells under alternate cycling and resting conditions at 1 mA $cm^{-2}$/1 mAh $cm^{-2}$. (g) Cycling performances at 2 mA $cm^{-2}$/6 mAh $cm^{-2}$. (h) Comparison of CPC with the other reported cells. In situ optical microscopy observation after different Zn stripping/plating cycles for (i) VGPL@Zn and (j) bare Zn electrodes.

evaluating cycling durability. This methodology reliably validates stability and efficiency by enabling continuous Zn stripping/plating cycles on metallic foils while monitoring reversibility through voltage profile analysis and cycle longevity measurements. As shown in Fig. 2b, the Zn//Zn symmetric cell initially displays severe polarization and undergoes an internal short circuit within 530 h at 5 mA $cm^{-2}$/1 mAh $cm^{-2}$ owing to uncontrolled dendrite formation. In stark contrast, the VGPL@Zn//VGPL@Zn symmetric cell demonstrates exceptional cycling stability, maintaining an ultralong lifespan of 5568 h with a remarkably low voltage hysteresis of merely 94 mV. This dramatic enhancement underscores the synergistic modulation of Zn stripping/plating behaviors, attributed to the interfacial regulation by CTAB and CMC on the anode surface. Additionally, the influence of VGPL thickness on cycling performance was investigated. The results indicate that an optimal thickness of 47 μm improves cycle life while minimizing increased $Zn^{2+}$ transport resistance and reduced concentration polarization (Fig. S9). Fig. 2c presents a comparison of the rate performances of symmetric cells across different current densities at a fixed areal capacity of 1 mAh

$cm^{-2}$. The VGPL@Zn anode consistently exhibits low polarization voltage and stable stripping/plating behavior, even at elevated current densities up to 10 mA $cm^{-2}$. The exchange current density of the VGPL@Zn anode, based on the Eq. S2, determined from voltage hysteresis measurements, measures 6.6 mA $cm^{-2}$ lower than the value of 7.7 mA $cm^{-2}$ observed for the bare Zn anode (Fig. S10). This reduced exchange current density effectively mitigates inactive Zn formation, suggesting improved interfacial kinetics and electrode uniformity. The cell voltage represents a critical metric for evaluating internal polarization phenomena in symmetric cells, arising from the combined effects of multiple electrochemical parameters, including interfacial ion concentration gradients and diffusion kinetics. Fig. 2d-e presents representative charge/discharge profiles from the 3rd cycle at various current densities, where discharge voltages (absolute values) are compared with charge voltages. The VGPL@Zn symmetric cell exhibits minimal polarization voltage with exceptionally flat plateaus, suggesting highly balanced stripping/plating kinetics [42]. Quantitative measurements of $Zn^{2+}$ transference numbers offer critical insight into interfacial ionic transport dynamics, where low values inevitably cause harmful concentration gradients and dendritic propagation. As depicted in Fig. S11, electrochemical impedance spectroscopy (EIS) and chronoamperometry (CA) measurements present that the VGPL@Zn electrode exhibits a higher $Zn^{2+}$ transference number (0.78) compared to unmodified Zn (0.27) based on the Eq. S3, indicating the protective layer's role in facilitating homogeneous $Zn^{2+}$ flux. To further assess the static corrosion resistance of the protective layer, symmetric cells were evaluated using an intermittent cycling protocol consisting of 20-h operational periods alternating with 10-h rest intervals (Fig. S12). A pronounced performance contrast is evident between the unmodified and engineered electrodes. The Zn anode exhibits rapid failure through short-circuiting within 63 h of operation. In marked contrast, the modified Zn electrode demonstrates exceptional cycling durability, sustaining stable electrochemical performance for 700 h with minimal voltage polarization variation across repeated cycling-rest intervals (Fig. 2f). To comparatively assess parasitic reaction inhibition, supplementary linear sweep voltammetry (LS*V*) and linear polarization measurements were systematically performed on the two anode configurations. The interfacial stabilization layer enables a cathodic shift of 30 mV in HER potential at 20 mA $cm^{-2}$ (from −0.11 V to −0.14 V) in Fig. S13, demonstrating effective suppression of competing hydrogen evolution at the protected Zn anode interface. Tafel plots in Fig. S14 further certify a much lower corrosion current density and a higher corrosion potential for the VGPL@Zn electrode. The VGPL@Zn electrode shows no detectable corrosion phases. Moreover, electrochemical cycling tests employing 20 μm Zn foil electrodes present enhanced cycling stability even under high depth-of-discharge (DOD) conditions. The VGPL@Zn symmetric cell exhibits outstanding electrochemical durability, maintaining stable operation for approximately 350 h at 52.2 % DOD with an areal capacity of 6 mAh $cm^{-2}$ (Fig. 2g). Conversely, the Zn//Zn symmetric cell fails prematurely, undergoing short-circuiting within 120 h under identical testing conditions. While conventional assessments of Zn stripping/plating stability typically rely on parameters such as current density, capacity density, and cycling duration, this study introduces cumulative plating capacity (CPC) as a more robust and comparable evaluation metric. As presented in Fig. 2h, the VGPL@Zn symmetric cell achieves a superior CPC value of 13,920 mAh $cm^{-2}$, surpassing some previously reported Zn-based symmetric cells in the literature (Table S1).

The above electrochemical data agree well with real-time morphological evolution captured by in situ optical microscopy at 10 mA $cm^{-2}$ operational conditions. Consistent with expectations, the engineered VGPL@Zn electrode preserved exceptional morphological stability, showing no detectable surface irregularities or dendritic protrusions during extended cycling (Fig. 2i). In contrast, the bare Zn foil developed severe surface irregularities within merely 20 cycles (Fig. 2j). These morphological protrusions disrupted local current distribution, triggering uncontrolled dendritic growth, ultimately resulting in catastrophic short-circuit failure. Confocal laser scanning microscopy (CLSM) analysis (Fig. S15) quantitatively characterized the surface evolution, manifesting significantly lower roughness development on the cycled VGPL@Zn electrode compared to the bare Zn electrode. In addition, comparative SEM analysis of post-cycled electrodes was conducted (Fig. S16), intuitively demonstrating morphological variations between the modified and unmodified anodes. After 20 cycles, disordered dendrites emerged on the bare Zn anode, while the VGPL@Zn surface kept its structural integrity. Subsequent cycling (100 cycles) produced large flake-like Zn deposits on the unmodified electrode, contrasting sharply with the progressively smoother VGPL@Zn surface that suppressed vertical Zn growth.

### 2.3. Investigation of Zn stripping behavior

The reversibility of the Zn stripping process is equally as critical as plating for achieving a long-lasting Zn metal anode. During stripping, uncontrolled and non-uniform Zn dissolution can lead to the formation of isolated, “dead” Zn particles that become electrically disconnected from the current collector. This irreversibility not only causes active material loss and rapid capacity fade but also leaves behind a highly corroded and irregular electrode surface. By optimizing the stripping process, $Zn^{2+}$ ions can be induced to dissolve uniformly from the electrode surface, thereby minimizing structural damage and preventing the accumulation of inactive Zn. This ensures that the electrode maintains a flat and dense morphology after multiple cycles, providing a sustainable foundation for subsequent highly reversible Zn deposition. Therefore, a well-modulated stripping mechanism is fundamental to maintaining electrode integrity, ensuring high CE over extended cycling [43,44]. The boosted cycling performance of Zn plating/stripping can be attributed to the effective interfacial engineering enabled by CMC and CTAB. During repeated stripping/plating cycles, the alternating electric field at the anode interface may dynamically modulate the interface chemical environment and the composition of the electrostatically self-assembled protective layer. Accordingly, this voltage-dependent composition evolution may influence interfacial mass transport. In situ Raman spectroscopy was first utilized to detect the interfacial chemistry at the Zn dissolution step. As anticipated, the disappearance of CTAB's characteristic $C–N^+$ peak at ~1480 $cm^{-1}$ (Fig. 3a) indicates positive electric field-induced dissociation of CTAB from the protective layer [45]. During the subsequent plating step, the characteristic peak reappeared. These observations demonstrate the dynamic structural reorganization behavior of the *V*GPL electrode (Fig. 3b). Guided by these findings, we conducted repeated Zn stripping/plating experiments using a three-electrode setup to quantify the voltage responses, focusing on elucidating CMC's role in modulating the Zn dissolution energy (Fig. S17). As illustrated in Fig. 3c, the calculated Zn dissolution energy from voltage profiles indicates smoother Zn stripping from the VGPL@Zn electrode (0.23 V) compared to bare Zn foil (0.59 V). In addition, density functional theory (DFT) calculations were performed by extracting a single Zn atom from distinct electrode surfaces (Fig. 3d-e). The Zn—Zn binding energy is determined to be −0.29 eV for the bare Zn anode, whereas this value decreases significantly to −0.07 eV for the CMC-modified interface (Fig. 3f). This striking reduction in binding energy unequivocally demonstrates stronger Zn dissolution tendency enabled by VGPL, which corresponds precisely with the observed trend of reducing overpotential [27].

The accumulation of by-products on electrode surfaces during cycling would elevate internal resistance and deteriorate battery performance. Excessive counter anions at the anode interface impede $Zn^{2+}$ transport and solvation, thus leading to irreversible side reactions during stripping processes [46]. As evidenced by our zeta potential measurements, CMC functionalization establishes a negatively charged surface on the Zn electrode. This negative surface potential is anticipated to electrostatically repel $SO_4^{2-}$ anions from the anode/electrolyte interface. The post-cycling X-ray diffraction (XRD) analysis (Fig. 3g)

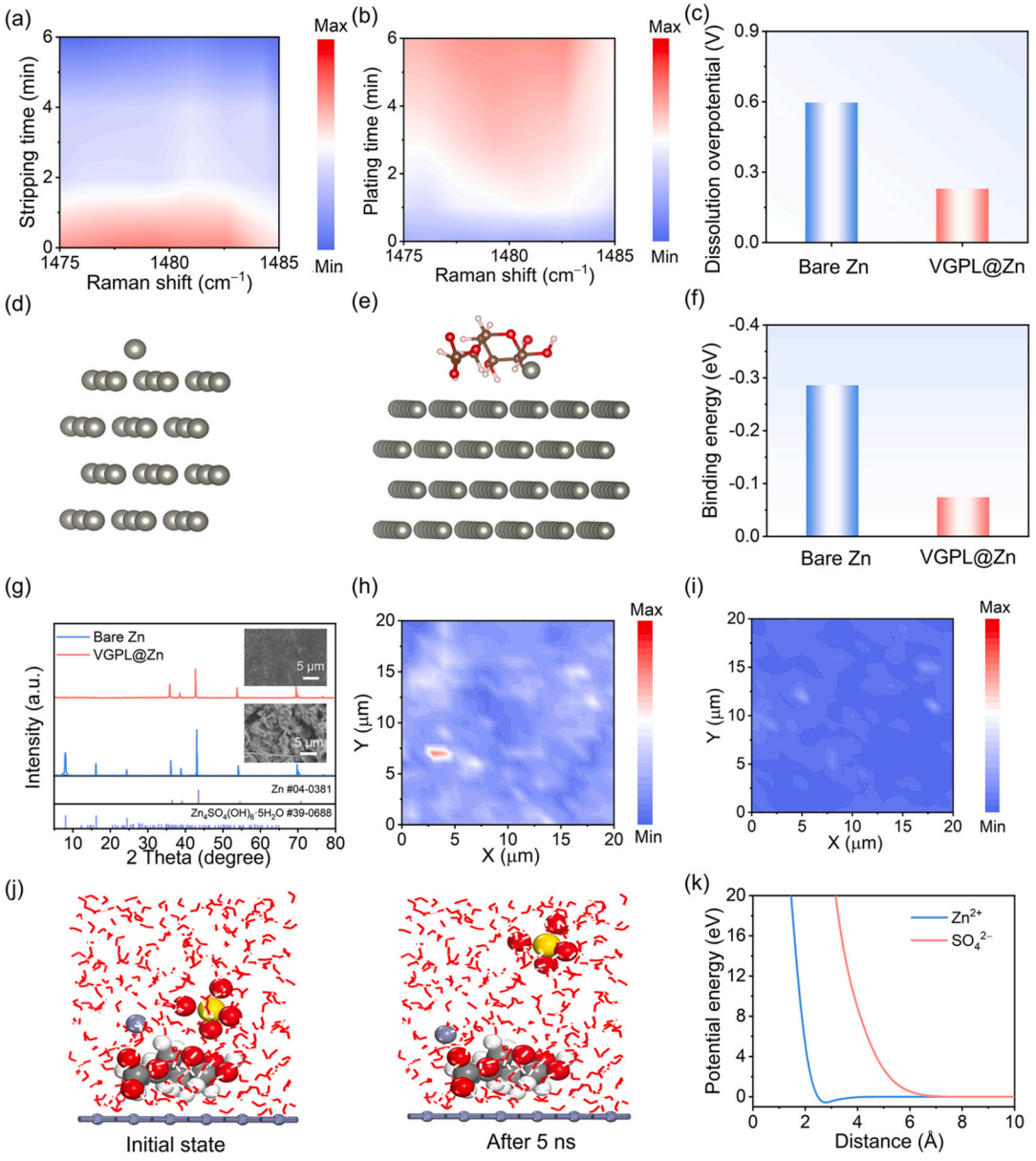


**Fig. 3.** In situ Raman spectra of the Zn/electrolyte interface under (a) stripping and (b) plating processes. (c) Dissolution overpotential of different anodes (first dissolution). The calculation models for extracting Zn from (d) bare Zn and (e) VGPL@Zn. (f) Zn—Zn binding energies in different anodes. (g) XRD patterns after cycling (the inset is the corresponding SEM images after cycling). Sulfide by-products Raman mapping images of cycled (h) bare Zn and (i) VGPL@Zn. (j) The snapshots of dynamic interactions. (k) The potential energy of CMC interacting with various ions.

reveals characteristic corrosion peaks at 8.1°, 16.2°, and 24.4° for the bare Zn anode, which are indexed to hydrated Zn hydroxide sulfate ($Zn_4SO_4(OH)_6{\cdot}5H_2O$, PDF #39–0688). In striking contrast, these impurity phases are completely absent in the XRD pattern of the VGPL@Zn electrode, demonstrating the effective suppression of corrosion products by the protective coating. As shown in the inset of Fig. 3g, the post-cycling SEM images align with the XRD results. The VGPL@Zn electrode has a smooth surface with no detectable by-products, in contrast to the bare Zn electrode, which shows pronounced by-product formation. Using the characteristic vibrational mode of $Zn_4SO_4(OH)_6{\cdot}5H_2O$ at 982.7 cm$^{-1}$, Raman mapping images manifest the spatial distribution of corrosion by-products [47]. As depicted in Fig. 3h, the cycled bare Zn electrode exhibits intense and heterogeneous signals corresponding to basic Zn sulfate, significantly increasing surface inhomogeneity. Conversely, the CMC-protected VGPL@Zn electrode presents nearly undetectable Raman signals (Fig. 3i), confirming the coating's exceptional effectiveness in suppressing by-product formation. Driven by the electron-rich character of its oxygen-containing groups, as confirmed by electrostatic potential (ESP) analysis in Fig. S18, the CMC-based layer serves as an effective barrier. By electrostatically excluding the charge-matched $SO_4^{2-}$ anions from the Zn anode interface during the stripping phase, it significantly stabilizes the electrode's electrochemical environment. Furthermore, we performed molecular dynamics (MD) simulations tracking ion trajectories to probe the interfacial ion dynamics during stripping. The simulation results display a clear anion migration preference, with $SO_4^{2-}$ exhibiting spontaneous redistribution away from the electrode/electrolyte interface within 5 ns (Fig. 3j). We quantitatively analyzed the interaction energetics between CMC and $SO_4^{2-}$ to elucidate their interfacial behavior. As shown in Fig. 3k, the potential energy between $Zn^{2+}$ and CMC reaches a distinct minimum at ~2.3 Å interatomic distance, maintaining favorable (negative) values even at larger separations. In stark contrast, the CMC-$SO_4^{2-}$ interaction remains energetically unfavorable (positive potential energy) across all distances. These computational results unambiguously demonstrate CMC's

dual functionality of selective $Zn^{2+}$ attraction and effective $SO_4^{2-}$ exclusion. Therefore, the CMC-derived protective layer, formed under positive electrode potential, constructs regulated ion channels for Zn stripping, which simultaneously inhibits sulfate-related parasitic reactions and enhances Zn dissolution kinetics.

### 2.4. Regulation of Zn deposition process

As a pivotal stage in the charge/discharge process, the controlled Zn deposition is essential in preventing the formation of Zn dendrites. Zn affinity at the anode surface critically determines both the desolvation behavior and nucleation mode. As demonstrated by the aforementioned in situ Raman spectroscopy, CTAB reincorporates into the protective layer during Zn deposition and participates in the electrochemical

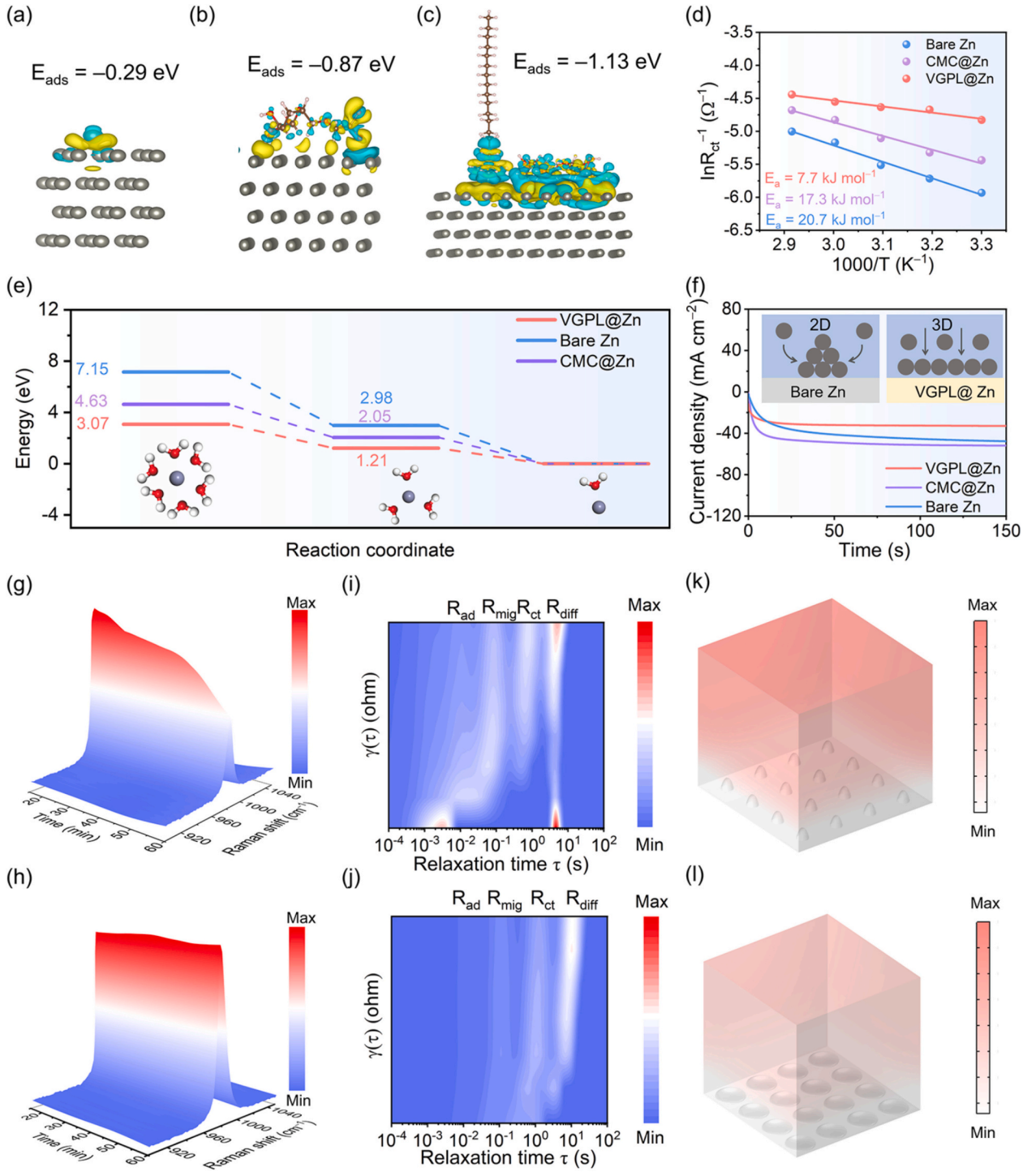


**Fig. 4.** The charge density difference and the corresponding adsorption energies of Zn absorbed on (a) bare Zn, (b) CMC@Zn, and (c) VGPL@Zn. (d) Desolvation energy calculated by the Arrhenius equation. (e) Comparison of the energy barriers encountered during the step-by-step desolvation process of $[Zn(H_2O)_6]^{2+}$. (f) CA curves of different electrodes. In situ Raman measurements during the Zn plating process for (g) bare Zn and (h) VGPL@Zn. The analysis of DRT of operando EIS for (i) bare Zn and (j) VGPL@Zn. Simulated $Zn^{2+}$ concentration distributions on (k) bare Zn and (l) VGPL@Zn.

reactions. DFT calculations were further utilized to identify the adsorption energy of $Zn^{2+}$ ions on different anode surfaces. Compared to bare Zn and CMC@Zn, the Zn binding energy on VGPL@Zn is −1.13 eV, confirming the effective enhancement of zincophilicity of the CMC-CTAB coated electrode (Fig. 4a-c). Furthermore, charge density difference analysis confirms significant interfacial charge transfer between CMC and Zn substrate, demonstrating that the oxygen-rich functional groups on CMC serve as effective zincophilic sites. Benefiting from both the intrinsic Zn affinity of CMC and the outward-oriented hydrophobic character of CTAB, this unique voltage-responsive interfacial protection layer is anticipated to provide thermodynamic driving force for $[Zn(H_2O)_6]^{2+}$ desolvation while simultaneously regulating $Zn^{2+}$ flux. The activation energy values ($E_a$) for desolvation processes were quantitatively determined through the Arrhenius formula. Temperature-dependent EIS results show a consistent reduction in charge transfer resistance ($R_{ct}$) values for the VGPL@Zn//VGPL@Zn cell relative to the Zn//Zn and CMC@Zn//CMC@Zn cells (Fig. S19), verifying more facile reaction kinetics at the functionalized interface. According to Eq. S4, the VGPL@Zn anode delivers a smaller $E_a$ value of 7.7 kJ $mol^{-1}$ compared with the bare Zn (20.7 kJ $mol^{-1}$) and CMC@Zn (17.3 kJ $mol^{-1}$) in Fig. 4d, evidencing enhanced desolvation kinetics and superior moisture-blocking capability. The sequential dehydration mechanism of $[Zn(H_2O)_6]^{2+}$ complexes was also elucidated through computational modeling (Fig. 4e). Energy profiles demonstrate that each dehydration step requires less energy for the optimal pathway occurring along the hydrophobic carbon chain of CTAB at the VGPL@Zn/electrolyte interface than at the unmodified Zn/electrolyte interface. This synergistic effect, arising from the combination of hydrophobic CTAB and zincophilic CMC, critically boosts the electrode's functionality by optimizing the desolvation of hydrated $Zn^{2+}$ ions and accelerating their interfacial transfer. This dual enhancement effectively regulates the Zn deposition kinetics, leading to a more homogeneous ion distribution and ultimately suppressing dendritic growth. Fig. S20 clearly illustrates the superior nucleation characteristics of the VGPL@Zn anode, which requires a far lower overpotential for Zn deposition (19.2 mV) compared to the untreated counterpart (42.5 mV). For the unmodified Zn anode, the CA measurements in Fig. 4f reveal a continuous current increase over the 150-s timeframe, characteristic of a two-dimensional (2D) diffusion-controlled deposition process [48]. Such kinetics emerge from non-uniform interfacial ion transport and the development of localized concentration gradients, ultimately leading to spatially irregular nucleation events. The CMC@Zn electrode exhibits a shorter 2D diffusion duration than the unmodified Zn, representing a moderated kinetic improvement. In contrast, the VGPL@Zn electrode displays fundamentally distinct deposition kinetics compared to unmodified Zn and CMC@Zn, exhibiting a brief initial period of 2D diffusion (only 30 s) before transitioning to stable 3D diffusion. This diffusion pattern transformation favors dendrite-free Zn deposition. The electric double layer capacitance (EDLC) was derived from cyclic voltammetry (CV) curves at different scan rates in symmetric cells (Fig. S21). A higher EDLC value was obtained for the VGPL@Zn electrode (8.9 mF $cm^{-2}$) compared to bare Zn (0.4 mF $cm^{-2}$) and CMC@Zn (6.2 mF $cm^{-2}$), confirming its superior interfacial reaction kinetics. This enhancement results from facilitated $Zn^{2+}$ transport and effective accumulation of $Zn^{2+}$ on the electrode surface.

Interfacial mass transport characterizations further corroborate the aforementioned optimization in Zn deposition behaviors. In situ Raman spectroscopy measurements focused on the $SO_4^{2-}$ vibration band (984 $cm^{-1}$) at the counter electrode provided a means to determine $Zn^{2+}$ ion concentrations. Near the bare Zn electrode, the $Zn^{2+}$ concentration experienced a pronounced attenuation within 20 min (Fig. 4g), reflecting significant inhomogeneity in the $Zn^{2+}$ spatial distribution during electrodeposition. Conversely, the modified interface maintained a remarkably uniform $Zn^{2+}$ concentration profile throughout the plating process (Fig. 4h). Moreover, the electrochemical relaxation characteristics of symmetric cells were systematically investigated through in situ EIS coupled with distribution of relaxation times (DRT) analysis (Fig. S22). This approach differentiates various electrochemical processes based on their characteristic relaxation time constants ($\tau$). The DRT analysis reveals four distinct relaxation processes characterized by $\tau$ values of $10^1$, $10^0$, $10^{-1}$, and $10^{-2}$ s, which were respectively assigned to $Zn^{2+}$ diffusion resistance ($R_{diff}$), $R_{ct}$, surface migration resistance ($R_{mig}$), and adsorption resistance ($R_{ad}$). The Zn//Zn cell exhibits an obvious increase in all $\tau$ values during initial plating stages, indicative of kinetically limited interfacial processes (Fig. 4i). This behavior likely originates from both insufficient active nucleation sites and rapid localized ion depletion near the electrode surface. The $\tau$ values obtained from the VGPL@Zn//VGPL@Zn cell deliver remarkable stability throughout the measurement period (Fig. 4j) [49]. This consistent temporal response confirms efficient mass transport characteristics at the electrode/electrolyte interface. To further corroborate our experimental findings, we conducted complementary COMSOL Multiphysics simulations to theoretically model the $Zn^{2+}$ concentration profiles across electrode/electrolyte interfaces. In Fig. 4k, a steep $Zn^{2+}$ concentration gradient developed within the interfacial region of the bare Zn anode, demonstrating a marked disparity between the rapid consumption rate during electrodeposition and the comparatively slow diffusion-limited replenishment from the electrolyte bulk. This kinetic instability fundamentally governs the development of the characteristic ion depletion layer at the electrode/electrolyte interface. Notably, the surface-modified Zn electrode demonstrates substantially reduced interfacial concentration gradients (Fig. 4l). Our computational simulations reveal that the synergistic effect between hydrophobic CTAB alkyl chains and zincophilic CMC functional groups enables enhanced $Zn^{2+}$ migration kinetics and more homogeneous deposition behavior relative to the bare Zn surface. These computational findings show remarkable consistency with our experimental measurements, validating the effectiveness of this interface engineering approach to rectify ion flux.

### 2.5. Application of full cells and pouch cells

Through systematic investigation of protective layer composition and interfacial $Zn^{2+}$ transport mechanisms during distinct Zn stripping/plating steps, it can be observed that CTAB exhibits voltage-dependent reversible adsorption/desorption behavior on CMC. Notably, this protective layer demonstrates ion transport regulation mechanisms functionally analogous to voltage-gated ion channels in some neuronal membranes, where transmembrane potential triggers selective ion permeability modulation. Inspired by this biomimetic mechanism, the protective layer regulates $Zn^{2+}$ flux in response to distinct voltages during charging/discharging processes. As a consequence, this bio-inspired voltage-gated protective layer simultaneously stabilizes Zn stripping and plating kinetics while enabling efficient ion rectification, thereby significantly enhancing the cycling durability of Zn anodes.

To further assess the reliability of VGPL@Zn for practical applications, the full ZIB was assembled by integrating the optimized anode with a ZVO cathode. The characteristic XRD diffraction peaks observed in Fig. S23 confirm the successful preparation of the ZVO cathode material [50]. Furthermore, SEM analysis reveals that the synthesized ZVO possesses a rod-like morphology (Fig. S24). The CV curves acquired at 1 mV $s^{-1}$ (Fig. 5a) display comparable redox peaks for both VGPL@Zn//ZVO and bare Zn//ZVO configurations, corresponding to $H^+/Zn^{2+}$ (de)intercalation processes. This observation confirms that the anode interface modification preserves the intrinsic energy storage mechanism of ZVO. Notably, the VGPL@Zn//ZVO full cell exhibits significantly enhanced current density relative to the Zn//ZVO counterpart, suggesting accelerated reaction kinetics and superior charge storage capacity. The CV curves exhibit negligible shape distortion across scan rates ranging from 1 to 5 mV $s^{-1}$ (Fig. S25), demonstrating the exceptional structural stability of the VGPL@Zn anode during repeated charge/discharge cycling. Fig. 5b displays the Nyquist plots and the

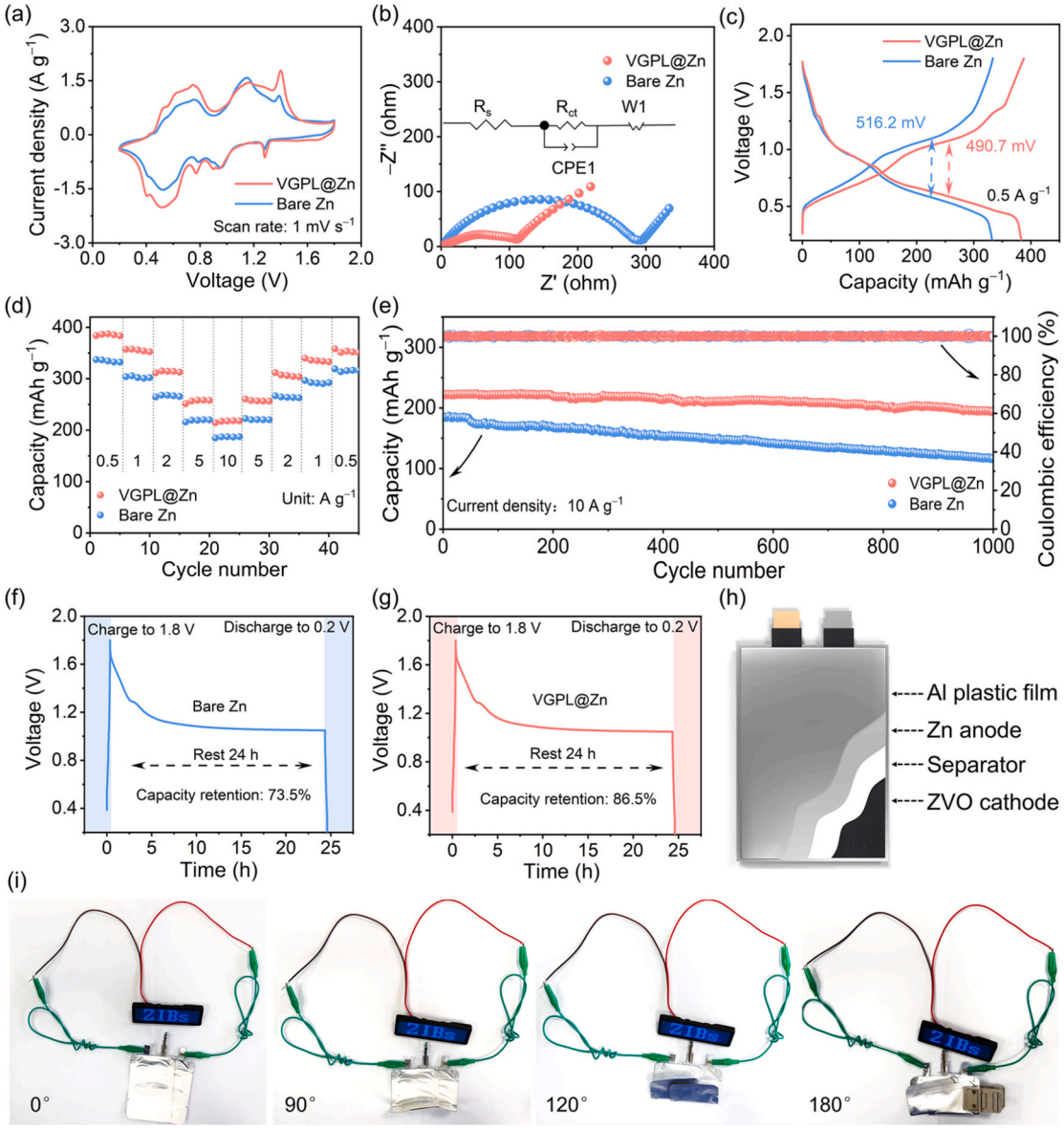


**Fig. 5.** Electrochemical performances of the VGPL@Zn//ZVO and Zn//ZVO full batteries. (a) CV curves at 1 mV $s^{-1}$. (b) Nyquist plots (inset: equivalent circuit diagram). (c) GCD profiles at 0.5 A $g^{-1}$. (d) Rate performances of the full batteries. (e) Cycling stability measurements at 10 A $g^{-1}$. Self-discharge behaviors of the (f) Zn//ZVO and (g) VGPL@Zn@ZVO full batteries. (h) Assembly schematic diagram of a pouch cell. (i) Pouch cells in series under different bending angles powering an LED array.

employed equivalent circuit. The high-frequency intercept is attributed to the series resistance ($R_s$). The prominent semicircle reflects the $R_{ct}$, and the low-frequency linear tail characterizes the $Zn^{2+}$ diffusion resistance. The EIS results demonstrate that the $R_{ct}$ value of the VGPL@Zn//ZVO full battery is 110 Ω, which is substantially lower than that of the conventional Zn//ZVO full battery (287 Ω). This notable reduction in $R_{ct}$ could be ascribed to the superior corrosion inhibition properties and enhanced ionic conductivity offered by the VGPL@Zn anode [51]. Evaluation of the ion diffusion resistance (σ) from the plot of Z' vs. $\omega^{-1/2}$ reveals a value of 7.7 Ω $s^{-1/2}$ for the VGPL@Zn//ZVO full cell, lower than the 16.2 Ω $s^{-1/2}$ for the Zn//ZVO cell. This lower σ is attributed to significantly accelerated $Zn^{2+}$ diffusion in the VGPL-modified system (Fig. S26). The energy storage performances of full batteries incorporating different anode materials were systematically evaluated based on galvanostatic charge/discharge (GCD) profiles (Fig. S27). As illustrated in Fig. 5c, the VGPL@Zn-based battery manifests significantly enhanced electrochemical performance at 0.5 A $g^{-1}$, delivering a higher discharge capacity (383.3 mAh $g^{-1}$) compared to the bare Zn-based battery (331.9 mAh $g^{-1}$) based on Eq. S5, along with diminished voltage polarization. Furthermore, rate capability tests demonstrate that the battery with the VGPL@Zn anode consistently maintains higher capacities across varying current densities from 0.5 to 10 A $g^{-1}$, underscoring its improved kinetic properties after ion flux rectification over the conventional Zn anode (Fig. 5d). The optimized ion transport kinetics enable both rapid charge/discharge processes and enhanced cycling durability. The VGPL@Zn//ZVO configuration yields remarkable capacity retention of 87.1 % after 1000 cycles at 10 A $g^{-1}$ (Fig. 5e), significantly outperforming the Zn//ZVO system (63.2 %). This superior performance originates from the exceptional electrochemical reversibility of the modified anode, as also confirmed by its outstanding average CE of 98.6 % throughout the cycling test. Besides, self-discharge characteristics were assessed through 24-h voltage monitoring at full charge. The bare Zn anode configuration shows significant capacity loss (retaining only 73.5 % when discharged to 0.2 V, Fig. 5f), in stark contrast to the VGPL@Zn system, which preserves 86.5 % capacity (Fig. 5g). We conducted performance evaluations in pouch

cell configurations to further validate the practical applicability of the VGPL@Zn anode (Fig. 5h). As evidenced in Fig. 5i, the assembled VGPL@Zn//ZVO pouch cell could power light-emitting diodes (LEDs) under different bending angles from 0° to 180°, demonstrating both operational reliability and inherent safety in practical applications. The experimental findings collectively showcase that the voltage-gated protective layer successfully realizes ion flux rectification, thereby simultaneously enhancing Zn anode utilization efficiency and electrochemical stability. This advancement significantly promotes the practical implementation of ZIB systems.

## 3. Conclusions

In summary, we successfully constructed a bioinspired voltage-gated protective layer that effectively rectified $Zn^{2+}$ ion flux to balance stripping and plating kinetics. During the stripping process, under the influence of the anode's surface positive electric field, CTAB becomes electrostatically detached while the remaining CMA matrix repels $SO_4^{2-}$ anions to minimize parasitic reactions and facilitates accelerated Zn dissolution kinetics. Upon electric field inversion at the plating step, CTAB re-adsorbs onto the CMC matrix, reforming a protective layer that stabilizes Zn deposition through component synergy. CTAB's hydrophobic alkyl chains enable the desolvation of hydrated $Zn^{2+}$ ions while CMC's oxygen-rich functional groups guide uniform nucleation. Capitalizing on these synergistic advantages, the VGPL@Zn symmetric cell delivers exceptional cycling stability, maintaining stable operation for over 5568 h at 5 mA $cm^{-2}$/1 mAh $cm^{-2}$. When configured as the full battery with the ZVO cathode, the system demonstrates remarkable long-term cyclability, retaining 87.1 % of its initial capacity after 1000 cycles at 10 A $g^{-1}$. This dynamic and reliable interface engineering offers great promise for achieving a robust Zn anode.

## CRediT authorship contribution statement

**Tianyu Zhang:** Writing – original draft, Validation, Data curation, Conceptualization. **Feng Yang:** Software, Methodology, Formal analysis, Data curation. **Yuexin Liu:** Software, Formal analysis. **Chengcheng Dong:** Visualization, Software. **Hongfei Wang:** Writing – original draft, Validation, Data curation, Conceptualization. **Yong Hu:** Writing – review & editing, Supervision, Project administration, Funding acquisition, Conceptualization.

## Declaration of competing interest

The authors declare that they have no known competing financial interests or personal relationships that could have appeared to influence the work reported in this paper.

## Acknowledgments

The authors appreciate the financial support by the National Natural Science Foundation of China (22272150 and 22502176), Zhejiang Provincial Natural Science of China (LZ23B030001), and Major Science and Technology Project of Jinhua City (2023-1-060). The calculations were carried out on high performance supercomputer of Zhejiang Normal University.

## Appendix A. Supplementary data

Supplementary data to this article can be found online at https://doi.org/10.1016/j.cej.2025.171212.

## Data availability

Data will be made available on request.

## References

[1] J.W. Choi, D. Aurbach, Promise and reality of post-lithium-ion batteries with high energy densities, Nat. Rev. Mater. 1 (2016) 16013, https://doi.org/10.1038/natrevmats.2016.13.
[2] Q. Xu, T. Li, Z. Ju, G. Chen, D. Ye, G.I.N. Waterhouse, Y. Lu, X. Lai, G. Zhou, L. Guo, K. Yan, X. Tao, H. Li, Y. Qiu, $Li_2ZrF_6$-based electrolytes for durable lithium metal batteries, Nature 637 (2025) 339–346, https://doi.org/10.1038/s41586-024-08294-z.
[3] C. Li, S. Jin, L.A. Archer, L.F. Nazar, Toward practical aqueous zinc-ion batteries for electrochemical energy storage, Joule 6 (2022) 1733–1738, https://doi.org/10.1016/j.joule.2022.06.002.
[4] S.W.D. Gourley, R. Brown, B.D. Adams, D. Higgins, Zinc-ion batteries for stationary energy storage, Joule 7 (2023) 1415–1436, https://doi.org/10.1016/j.joule.2023.06.007.
[5] L. Yuan, J. Hao, C.-C. Kao, C. Wu, H.-K. Liu, S.-X. Dou, S.-Z. Qiao, Regulation methods for the Zn/electrolyte interphase and the effectiveness evaluation in aqueous Zn-ion batteries, Energy Environ. Sci. 14 (2021) 5669–5689, https://doi.org/10.1039/D1EE02021H.
[6] S. Huang, S. He, S. Huang, X. Zeng, Y. Li, H. Noor, X. Hou, Molecular crowding agent modified polyanionic gel electrolyte for zinc ion batteries operating at 100 °C, Adv. Funct. Mater. 35 (2024) 2419153, https://doi.org/10.1002/adfm.202419153.
[7] S. Huang, S. He, Y. Li, S. Wang, X. Hou, Hydrogen bond acceptor lined hydrogel electrolyte toward dendrite-free aqueous Zn ion batteries with low temperature adaptability, Chem. Eng. J. 464 (2023) 142607, https://doi.org/10.1016/j.cej.2023.142607.
[8] A. Bayaguud, X. Luo, Y. Fu, C. Zhu, Cationic surfactant-type electrolyte additive enables three-dimensional dendrite-free zinc anode for stable zinc-ion batteries, ACS Energy Lett. 5 (2020) 3012–3020, https://doi.org/10.1021/acsenergylett.0c01792.
[9] Q. Deng, S. You, W. Min, Y. Xu, W. Lin, J. Lu, C. Yang, Polymer molecules adsorption-induced zincophilic-hydrophobic protective layer enables highly stable Zn metal anodes, Adv. Mater. 36 (2024) 2312924, https://doi.org/10.1002/adma.202312924.
[10] Y. Lin, Z. Mai, H. Liang, Y. Li, G. Yang, C. Wang, Dendrite-free Zn anode enabled by anionic surfactant-induced horizontal growth for highly-stable aqueous Zn-ion pouch cells, Energy Environ. Sci. 16 (2023) 687–697, https://doi.org/10.1039/D2EE03528F.
[11] Y. Wang, Y. Kong, T. Zhang, C. Chen, H. Wang, Y. Hu, Fluorine-functionalized chemistry toward stable Zn anode in aqueous Zn-ion batteries, Adv. Energy Mater. 15 (2025) 2502353, https://doi.org/10.1002/aenm.202502353.
[12] H. Wang, W. Ye, B. Yin, K. Wang, M.S. Riaz, B.B. Xie, Y. Zhong, Y. Hu, Modulating cation migration and deposition with xylitol additive and oriented reconstruction of hydrogen bonds for stable zinc anodes, Angew. Chem. Int. Ed. 62 (2023) e202218872, https://doi.org/10.1002/anie.202218872.
[13] S. Huang, S. Huang, S. He, H. Noor, L. Zhao, X. Hou, H. Chen, A functional MXene/cellulose nanofibers separator for high-performance dendrite-free zinc anode under harsh conditions, Surf. Interfaces 51 (2024) 104735, https://doi.org/10.1016/j.surfin.2024.104735.
[14] W. Hu, S. Huang, S. He, Y. Zheng, W. Zhou, H. Cui, H. Noor, X. Hou, Manipulating $Zn^{2+}$ solvation sheath utilizing an antisolvent under high temperature conditions for high zinc anode reversibility, J. Energy Storage 83 (2024) 110488, https://doi.org/10.1016/j.est.2024.110488.
[15] R. Qin, Y. Wang, L. Yao, L. Yang, Q. Zhao, S. Ding, L. Liu, F. Pan, Progress in interface structure and modification of zinc anode for aqueous batteries, Nano Energy 98 (2022) 107333, https://doi.org/10.1016/j.nanoen.2022.107333.
[16] Y. Zhu, G. Liang, X. Cui, X. Liu, H. Zhong, C. Zhi, Y. Yang, Engineering hosts for Zn anodes in aqueous Zn-ion batteries, Energy Environ. Sci. 17 (2024) 369–385, https://doi.org/10.1039/D3EE03584K.
[17] C. Nie, G. Wang, D. Wang, M. Wang, X. Gao, Z. Bai, N. Wang, J. Yang, Z. Xing, S. Dou, Recent progress on Zn anodes for advanced aqueous zinc-ion batteries, Adv. Energy Mater. 13 (2023) 2300606, https://doi.org/10.1002/aenm.202300606.
[18] Z. Zhao, R. Wang, C. Peng, W. Chen, T. Wu, B. Hu, W. Weng, Y. Yao, J. Zeng, Z. Chen, P. Liu, Y. Liu, G. Li, J. Guo, H. Lu, Z. Guo, Horizontally arranged zinc platelet electrodeposits modulated by fluorinated covalent organic framework film for high-rate and durable aqueous zinc ion batteries, Nat. Commun. 12 (2021) 6606, https://doi.org/10.1038/s41467-021-26947-9.
[19] X. Zhong, M. Zhou, T. Xu, X. Zhuge, Z. Luo, K. Luo, L. Pan, Superhydrophobic $SiO_2$ coating layer enabling stable and reversible Zn anode for aqueous Zn-ion batteries, Appl. Surf. Sci. 654 (2024) 159406, https://doi.org/10.1016/j.apsusc.2024.159406.
[20] Y. Li, S. Yang, H. Du, Y. Liu, X. Wu, C. Yin, D. Wang, X. Wu, Z. He, X. Wu, A stable fluoride-based interphase for a long cycle Zn metal anode in an aqueous zinc ion battery, J. Mater. Chem. A 10 (2022) 14399–14410, https://doi.org/10.1039/D2TA03550B.
[21] Y. Chen, B. Yin, Y. Zeng, H. Wang, B.-B. Xie, D. Luan, Y. Hu, X.W. Lou, Ion-dipole interaction manipulated bilateral interface chemistry for deep rechargeability and high redox activity of Zn-organic batteries, Chem 11 (2025) 102411, https://doi.org/10.1016/j.chempr.2025.102411.
[22] H. Lu, B. Yin, T. Zhang, Y. Shao, J. Zhong, H. Wang, B.-B. Xie, Y. Zhong, Y. Hu, Dual-additive synergistic complementation electrolyte engineering with "job-sharing" modulation mechanism for long-lifespan Zn-iodine batteries, ACS Appl. Mater. Interfaces 17 (2025) 21234–21245, https://doi.org/10.1021/acsami.5c00459.

[23] F. Yang, C. Tian, L. Bai, T. Zhang, H. Wang, J. Ning, Y. Hu, Hierarchical array hosts with concave spatial confinement and zincophilic seed mediated growth for dendrite-free Zn metal anode, Compos. Part B Eng. 301 (2025) 112528, https://doi.org/10.1016/j.compositesb.2025.112528.
[24] C. Tian, H. Wang, L. Xie, Y. Zhong, Y. Hu, Arrays of hierarchical zincophilic nanorods with trapping-and-leveling deposition for ultrastable Zn metal anodes, Adv. Energy Mater. 14 (2024) 2400276, https://doi.org/10.1002/aenm.202400276.
[25] Y. Zhou, J. Xia, J. Di, Z. Sun, L. Zhao, L. Li, Y. Wu, L. Dong, X. Wang, Q. Li, Ultrahigh-rate Zn stripping and plating by capacitive charge carriers enrichment boosting Zn-based energy storage, Adv. Energy Mater. 13 (2023) 2203165, https://doi.org/10.1002/aenm.202203165.
[26] Z. Shi, M. Yang, Y. Ren, Y. Wang, J. Guo, J. Yin, F. Lai, W. Zhang, S. Chen, H. N. Alshareef, T. Liu, Highly reversible Zn anodes achieved by enhancing ion-transport kinetics and modulating Zn (002) deposition, ACS Nano 17 (2023) 21893–21904, https://doi.org/10.1021/acsnano.3c08197.
[27] Z. Li, Z. Shu, Z. Shen, Y. Liu, Y. Ji, L. Luo, R. Li, Y. Cai, H. Ian, J. Xie, G. Hong, Dissolution mechanism for dendrite-free aqueous zinc-ions batteries, Adv. Energy Mater. 14 (2024) 2400572, https://doi.org/10.1002/aenm.202400572.
[28] D. Tang, X. Zhang, D. Han, C. Cui, Z. Han, L. Wang, Z. Li, B. Zhang, Y. Liu, Z. Weng, Q.-H. Yang, Switching hydrophobic interface with ionic valves for reversible zinc batteries, Adv. Mater. 36 (2024) 2406071, https://doi.org/10.1002/adma.202406071.
[29] K. Qi, P. Liang, S. Wei, H. Ao, X. Ding, S. Chen, Z. Fan, C. Wang, L. Song, X. Wu, C. Wu, Y. Zhu, Trade-off between $H_2O$-rich and $H_2O$-poor electric double layers enables highly reversible Zn anodes in aqueous Zn-ion batteries, Energy Environ. Sci. 17 (2024) 2566–2575, https://doi.org/10.1039/D4EE00147H.
[30] S.D. Pu, B. Hu, Z. Li, Y. Yuan, C. Gong, Z. Ning, C. Chau, S. Yang, S. Zhang, L. Pi, Y. T. Tang, J. Yue, T.J. Marrow, X. Gao, P.G. Bruce, A.W. Robertson, Decoupling, quantifying, and restoring aging-induced Zn-anode losses in rechargeable aqueous zinc batteries, Joule 7 (2023) 366–379, https://doi.org/10.1016/j.joule.2023.01.010.
[31] J. Xu, P. Han, Y. Jin, H. Lu, B. Sun, B. Gao, T. He, X. Xu, N. Pinna, G. Wang, Hybrid molecular sieve-based interfacial layer with physical confinement and desolvation effect for dendrite-free zinc metal anodes, ACS Nano 18 (2024) 18592–18603, https://doi.org/10.1021/acsnano.4c04632.
[32] H. Li, S. Li, R. Hou, Y. Rao, S. Guo, Z. Chang, H. Zhou, Recent advances in zinc-ion dehydration strategies for optimized Zn-metal batteries, Chem. Soc. Rev. 53 (2024) 7742–7783, https://doi.org/10.1039/D4CS00343H.
[33] F. Ling, L. Wang, F. Liu, M. Ma, S. Zhang, X. Rui, Y. Shao, Y. Yang, S. He, H. Pan, X. Wu, Y. Yao, Y. Yu, Multi-scale structure engineering of $ZnSnO_3$ for ultra-long-life aqueous zinc-metal batteries, Adv. Mater. 35 (2023) 2208764, https://doi.org/10.1002/adma.202208764.
[34] C. Li, Q. Shao, K. Luo, Y. Gao, W. Zhao, N. Cao, S. Du, X. Jin, P. Zou, X. Zang, A lean-zinc and zincophilic anode for highly reversible zinc metal batteries, Adv. Funct. Mater. 33 (2023) 2305204, https://doi.org/10.1002/adfm.202305204.
[35] S. Yoo, D.R. Mittelstein, R.C. Hurt, J. Lacroix, M.G. Shapiro, Focused ultrasound excites cortical neurons via mechanosensitive calcium accumulation and ion channel amplification, Nat. Commun. 13 (2022) 493, https://doi.org/10.1038/s41467-022-28040-1.
[36] T. Yan, J. Liu, Transmembrane ion channels: from natural to artificial systems, Angew. Chem. Int. Ed. 64 (2025) e202416200, https://doi.org/10.1002/anie.202416200.
[37] P. Zhai, R. Shao, C. Zeng, S. Qu, F. Pei, Y. Li, W. Yang, Robust ion-rectifying polymer electrolyte membrane for high-rate solid-state lithium metal batteries, Chem. Eng. J. 473 (2023) 144840, https://doi.org/10.1016/j.cej.2023.144840.
[38] Y. Xing, B. Zhang, Q. Niu, G. Ji, Enhanced adsorption of polystyrene nanoplastics by cetyltrimethylammonium bromide surface-modified magnetic rice straw biochar: efficient performance and adsorption mechanisms, Sep. Purif. Technol. 344 (2024) 127264, https://doi.org/10.1016/j.seppur.2024.127264.
[39] R. Wang, J. Wan, H. Guo, B. Tian, S. Li, J. Li, S. Liu, T.D. James, Z. Chen, "All-in-one" carbon dots-based catalyst for converting $CO_2$ to cyclic carbonates, Carbon 211 (2023) 118118, https://doi.org/10.1016/j.carbon.2023.118118.
[40] Y. Liu, J. Zhang, Y. Liu, M. Zhang, Z. Pan, K. Cai, Controllable design of metal-organic framework-derived vanadium oxynitride for high-capacity and long-cycle aqueous Zn-ion batteries, Small 20 (2024) 2401922, https://doi.org/10.1002/smll.202401922.
[41] S. Tao, C. Zhang, J. Zhang, Y. Jiao, M. Li, W. Lin, L. Ran, B. Clement, M. Lyu, I. Gentle, L. Wang, R. Knibbe, A hydrophobic and fluorophilic coating layer for stable and reversible aqueous zinc metal anodes, Chem. Eng. J. 446 (2022) 136607, https://doi.org/10.1016/j.cej.2022.136607.
[42] R. Guo, X. Liu, K. Ni, F. Xia, H. Zhang, Y. Liu, X. Dai, L. Shi, X. Wang, C. Han, L. Mai, C. Niu, Non-destructive stripping electrochemistry enables long-life zinc metal batteries, Energy Environ. Sci. 18 (2025) 2353–2364, https://doi.org/10.1039/D4EE05044D.
[43] H.B. Chen, H. Meng, T.R. Zhang, Q. Ran, J. Liu, H. Shi, G.F. Han, T.H. Wang, Z. Wen, X.Y. Lang, Q. Jiang, Dynamic molecular interphases regulated by trace dual electrolyte additives for ultralong-lifespan and dendrite-free zinc metal anode, Angew. Chem. Int. Ed. 63 (2024) e202402327, https://doi.org/10.1002/anie.202402327.
[44] Z. Liu, G. Xu, Y. Zhang, M. Li, H. Li, J. Zhang, J. Hu, T. Lin, N. Zhang, Unveiling zinc stripping and molecular engineering for high-performance zinc anode, Angew. Chem. Int. Ed. 64 (2025) e202501960, https://doi.org/10.1002/anie.202501960.
[45] I. Petreanu, N. Violeta-Carolina, E. Stanica, I. Ciprian, M. Teodorescu, Structural characterization of silica and amino-silica nanoparticles by fourier transform infrared (FTIR) and Raman spectroscopy, Anal. Lett. 56 (2023) 390–403, https://doi.org/10.1080/00032719.2022.2083144.
[46] M. Zhang, S. Li, R. Tang, C. Sun, J. Yang, G. Chen, Y. Kang, Z. Lv, Z. Wen, C.C. Li, J. Zhao, Y. Yang, Stabilizing Zn/electrolyte interphasial chemistry by a sustained-release drug inspired indium-chelated resin protective layer for high-areal-capacity Zn//$V_2O_5$ batteries, Angew. Chem. Int. Ed. 63 (2024) e202405593, https://doi.org/10.1002/anie.202405593.
[47] D. Wang, N. Zhang, Y. Zhang, L. Chang, H. Tang, W. Zhang, Q. Zhu, Electric field sponge effect of conducting polymer interphases boosts the kinetics and stability of zinc metal anodes, Adv. Energy Mater. 15 (2025) 2404090, https://doi.org/10.1002/aenm.202404090.
[48] M. Cui, L. Yu, J. Hu, S. He, C. Zhi, Y. Huang, Tailored polymer-inorganic bilayer SEI with proton holder feature for aqueous Zn metal batteries, Angew. Chem. Int. Ed. 64 (2025) e202423531, https://doi.org/10.1002/anie.202423531.
[49] S. Chen, K. Ouyang, Y. Liu, H. Qin, M. Cui, A. Liu, Y. Wang, K. Zhang, Y. Huang, Strong metal-support interaction to invert hydrogen evolution overpotential of Cu coating for high-coulombic-efficiency stable Zn anode in aqueous Zn-ion batteries, Adv. Mater. 37 (2025) 2417775, https://doi.org/10.1002/adma.202417775.
[50] T. Wang, Q. Xi, K. Yao, Y. Liu, H. Fu, V.S. Kavarthapu, J.K. Lee, S. Tang, D. Fattakhova-Rohlfing, W. Ai, J.S. Yu, Surface patterning of metal zinc electrode with an in-region zincophilic interface for high-rate and long-cycle-life zinc metal anode, Nano-Micro Lett. 16 (2024) 112, https://doi.org/10.1007/s40820-024-01327-2.
[51] L. Wang, B. Zhang, W. Zhou, Z. Zhao, X. Liu, R. Zhao, Z. Sun, H. Li, X. Wang, T. Zhang, H. Jin, W. Li, A. Elzatahry, Y. Hassan, H.J. Fan, D. Zhao, D. Chao, Tandem chemistry with janus mesopores accelerator for efficient aqueous batteries, J. Am. Chem. Soc. 146 (2024) 6199–6208, https://doi.org/10.1021/jacs.3c14019.